Landslides (2018) 15:551–564
DOI 10.1007/s10346-017-0929-1
Received: 27 July 2017
Accepted: 28 November 2017
Published online: 12 December 2017

Chong Xu · Siyuan Ma · Zhibiao Tan · Chao Xie · Shinji Toda · Xueqiang Huang

Landslides triggered by the 2016 Mj 7.3 Kumamoto, Japan, earthquake

Abstract The aim of this study is to establish a detailed and complete inventory of the landslides triggered by the Mj 7.3 (Mw 7.0) Kumamoto, Japan, earthquake sequence of 15 April 2016 (16 April in JST). Based on high-resolution (0.5–2 m) optical satellite images, we delineated 3,467 individual landslides triggered by the earthquake, occupying an area of about 6.9 km^2. Then they were validated by aerial photographs with very high-resolution (better than 0.5 m) and oblique field photos. Of them, 3,460 landslides are distributed in an elliptical area about 6000 km^2, with a NE-SW directed 120-km-long long axis and a 60-km-long NW-SE trending short axis. Most of the landslides are shallow, disrupted falls and slides, with a few flow-type slides and rock and soil avalanches. The analysis of correlation between the landslides and several control factors shows the areas of elevation 1000–1200 m, stratum of Q_3-H*vf*, seismic intensity VIII and VIII+, and peak ground acceleration (PGA) 0.4–0.6 g register the highest landslide abundance. This study also discussed the relationship between the spatial pattern of the landslides and the seismotectonic structure featured by a strike-slip fault with a normal component and the volcanism in the study area.

Keywords Earthquake · Coseismic landslides · Spatial distribution · Visual interpretation

Introduction

Detailed and complete inventories are of great significance in many aspects of study on seismic landslides, such as mechanisms, spatial pattern, and hazard assessment of landslides. They are also useful for understanding characteristics of earthquakes, surface ruptures, and seismogenic faults. Therefore, this subject has received much attention in recent years. Researchers have established detailed landslide databases and inventories related to dozens of major earthquakes, such as the 2015 Gorkha, Nepal Mw7.8 (British Geological Survey et al. 2015; Gnyawali et al. 2016; Kargel et al. 2016; Xu et al. 2016a; Xu et al. 2017), 2014 Ludian, China Mw6.1 (Xu et al. 2014a), the 2013 Minxian, China Mw5.9 (Xu et al. 2014b; Tian et al. 2016), 2013 Lushan, China Mw6.6 (Xu et al. 2015a, b), the 2010 Yushu, China Mw 6.9 (Xu et al. 2013; Xu and Xu 2014), Port-au-Prince, Haiti Mw 7.0 (Xu et al. 2014c), the 2008 Wenchuan, China Mw7.9 (Xu et al. 2014d), 2002 Denali, Alaska Mw7.9 (Gorum et al. 2014), 1999 Chi-chi, Taiwan, China Mw7.6 (Liao and Lee 2000), and 1994 Northridge, America Mw6.7 quake (Harp and Jibson 1995). Apparently this subject will continue to be a focused issue of landslide research in the future.

The 2016 Kumamoto, Japan earthquake sequence began with an Mj 6.5 foreshock of 12:26 (UTC Time) on 14 April 2016 and reached its climax of the Mj 7.3 mainshock of 16:25 (UTC Time) on April 15, 2016, which caused widespread damage throughout central Kyushu Island of Japan, killing 50 people. Although the topographic relief and hillslope steepness of the affected area are relatively moderate, the earthquake generated a lot of landslides resulting in serious damages, such as buried roads, blocking rivers, and liquefactions. According to several reports (Goda et al. 2016; Kayen et al. 2016; NZSEE 2016; Okumura 2016), four landslides triggered by the quake directly caused at least ten fatalities. The quake also result in the strength weakening of the slopes in the affected area, thus the susceptibility of landslides after the quake may increase and new landslides would be a major hazard under subsequent strong aftershocks or rainfalls. Therefore, a detailed and complete inventory of landslides triggered by the Kumamoto earthquake is a support for recovery and reconstruction, landslide prevention, and mitigation in the affected area.

After this event, National Research Institute for Earth Science and Disaster Resilience (NIED) (http://www.bosai.go.jp/mizu/dosha.html) and Disaster Prevention Research Institute at Kyoto University (http://www.slope.dpri.kyoto-u.ac.jp/disaster_reports/2016KumamotoEq/2016KumamotoEq2.html) have carried out investigations and prepared several maps of the earthquake-triggered landslides, respectively. Disaster Prevention Research Institute at Kyoto University delineated 336 coseismic landslides in the Aso volcano area. NIED released several versions of coseismic landslide inventory including 1471, 1212, and 1744 coseismic landslides in the Aso volcano area and two larger affected areas on April 29, May 2, and June 27, 2016, respectively (http://www.bosai.go.jp/mizu/dosha.html). However, none of these results cover the whole earthquake-affected area, and many moderate- or small-scale landslides were probably omitted, which makes it difficult to perform a more comprehensive study of the coseismic landslides by this quake.

This study attempted to establish a more detailed and complete inventory of the landslides triggered by the Kumamoto earthquake sequence. Based on high-resolution (0.5–2 m) optical satellite images before and after the shock, with the validation using ortho-aerial photographs with very high-resolution (better than 0.5 m) and oblique field photos, we delineated 3467 individual landslides triggered by this event. Results show the landslides are almost distributed in an elliptical area about 6000 km^2, with a NE-SW directed 120-km-long long axis and a 60-km-long NW-SE short axis. Most of the landslides are shallow, disrupted landslides with a few flow-type landslides and rock and soil avalanches. These coseismic landslides show a strong spatially non-uniform pattern; most of which (about 2900 pieces) occurred in the Aso volcano area about 500 km^2. The correlations between coseismic landslides and several condition factors, such as topographic, geologic, and seismic factors, were also analyzed in this work.

Geologic setting and earthquake deformation

The Kumamoto earthquake sequence occurred about 300 km northwest of the Ryukyu trench, where the Philippine Sea plate was northwestward subducting beneath the Eurasia plate (Fig. 1a). The main shock epicenter is located in the upper crust beneath the Kumamoto-Aso region of Kyushu Island in southwest Japan, where exist Paleozoic and Mesozoic rocks, island arc plutonism/volcanism, tectonic accretion, and metamorphism, as well as the filling of back-arc and fore-arc basins (Kayen et al. 2016). The

affected area is featured by volcanic extensional structure with predominant EW compression (Okumura 2016). Mapped active faults in the Kyushu island generally trend east-west for normal faults or northeast-southwest for strike-slip faults (Fig.1b). The Kumamoto earthquake was generated by the slipping of the Futagawa-Hinagu fault zone (FHFZ), which is composed of two main active faults, the Futagawa and Hinagu faults striking NE–SW, dominated by right-lateral strike-slip with an uplift component to the southeast (Fig. 1b). The Futagawa fault (FF) extends for ~ 64 km while the Hinagu fault (HF) extends for ~ 81 km, respectively. The Hinagu fault merges obliquely with the Futagawa fault in the northeast. Only 13 earthquakes of M5 + were recorded at shallow depth (< 50 km) within 100 km to the epicenter of the 2016 Kumamoto event over the preceding century (US Geological Survey 2016).

The Kumamoto earthquake resulted in regional strain change (Sano et al. 2016) and extensional open fissures (Tsuji et al. 2017). Coseismic surface ruptures caused by this event were detected by several methods, such as field reconnaissance (Kayen et al. 2016; Sugito et al. 2016; Toda et al. 2016; Goto et al. 2017), InSAR (Fujiwara et al. 2016; Himematsu and Furuya 2016) and LiDAR data (Moya et al. 2017). The surface rupture zone visible is ~ 35 km long mainly along FHFZ and newly identified faults ~ 5 km long on the western side of the Aso caldera, where the faults diminish. To southwest, the surface ruptures appeared to have extended further west out of the main FHFZ into the Kumamoto plain (Goto et al. 2017). The northeastward propagation of the coseismic ruptures terminates in the Aso caldera (Miyakawa et al. 2016). In addition, a set of ~ 10-km-long normal fault scarps dipping to the northwest were observed along the previously mapped Idenokuchi fault about 1.5 km southeast of and subparallel to the Futagawa fault (Toda et al. 2016). Both the maximum of coseismic horizontal displacement and subsidence are about 2 m (Moya et al. 2017). As of October 31, 2016, National Research Institute for Earth Science and Disaster Resilience (NIED, http://www.fnet.bosai.go.jp/event/search.php?LANG=en) recorded 218 Mj 3.5 + earthquakes, including 25 foreshocks and 192 aftershocks. The two largest foreshocks are the April 14, 2016, Mj 6.5 event at 12:26 UTC (32.7417°N, 130.8087°E) and the April 14, 2016, Mj 6.4 event at 15:03 UTC (32.7007°N, 130.7777°E). The largest aftershocks are two Mj 5.9 events occurred at 16:45 (32.8632°N, 130.899°E) and 18:03 UTC (32.9638°N, 131.0868°E) on April, 15, 2016, respectively. The largest Mj 6.5 foreshock was generated by a right-lateral strike-slip fault, northeast of the Hinagu fault. The Mj 7.3 (Mw 7.0) mainshock is a

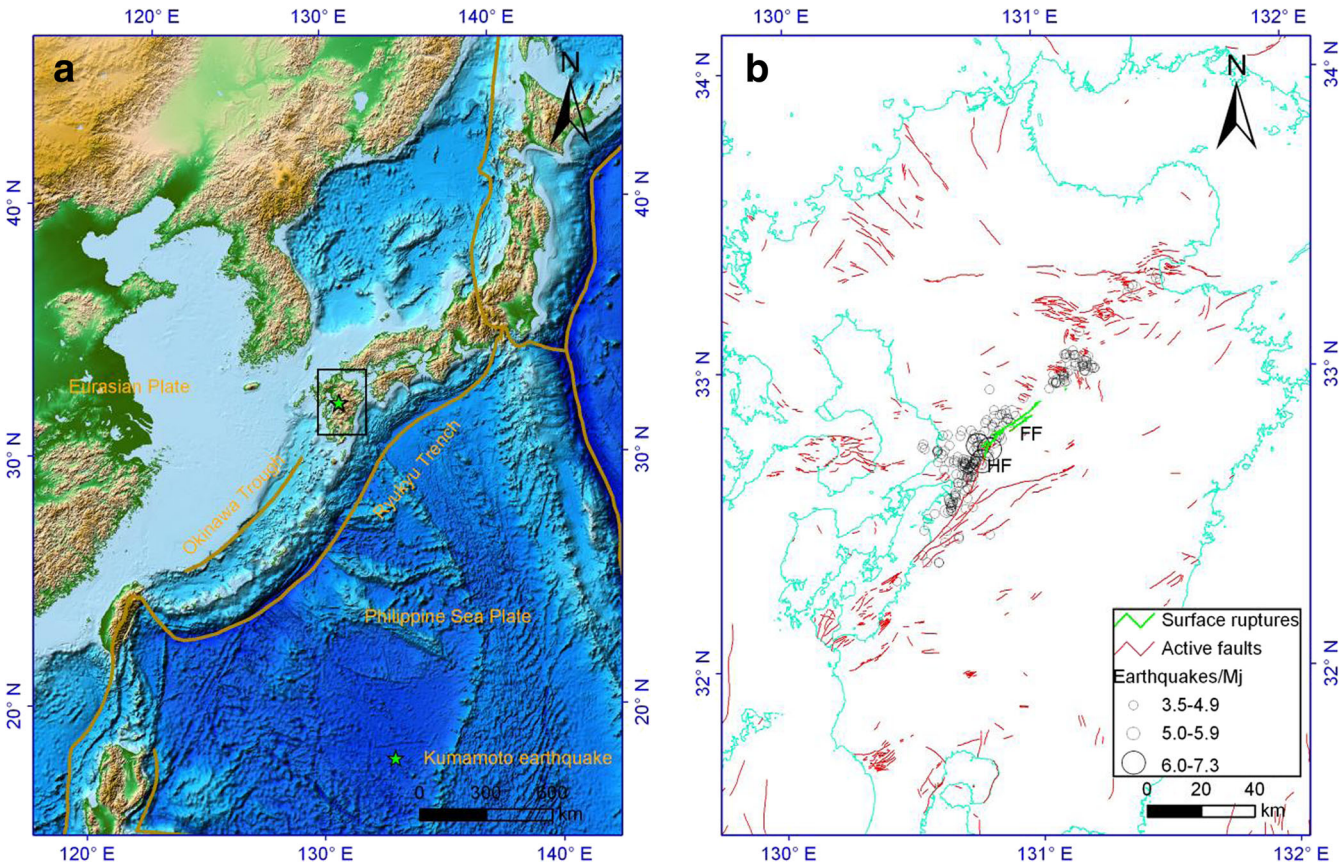

Fig. 1 Tectonic setting of the 2016 Kumamoto earthquake. (**a**) Tectonic setting of the area. (**b**) Active faults in Kyushu and the Kumamoto earthquake sequence. The box in panel A shows the range of panel B. HF, Hinagu fault; FF, Futagawa fault. The plate boundaries and topographic background on panel A are from USGS kml file (www.usgs.gov) and National Geophysical Data Center, NOAA (Amante and Eakins 2009), respectively. Active faults on panel B are modified from Active Fault Research Group (Active Fault Research Group 1991) and Kato et al. (Kato et al. 2016). The earthquake sequence data is from National Research Institute for Earth Science and Disaster Resilience (NIED, http://www.fnet.bosai.go.jp/event/search.php?LANG=en). The figure is derived from ArcGIS 9.2 platform (http://www.esrichina.com.cn/softwareproduct/ArcGIS)

right-lateral strike-slip with a normal faulting component, located at the Futagawa fault zone, which is the northeastern neighbor of the Hinagu fault zone (Active Fault Research Group 1991; Nakata and Imaizumi 2002; Asano and Iwata 2016; Matsumoto et al. 2016). Overall, the Kumamoto earthquake sequence shows unusual and puzzling spatial gaps after the main shock (Kato et al. 2016; Uchide et al. 2016). The near-field strong motion record shows the mainshock is characterized by large ground accelerations and short-time duration (Furumura 2016).

Data and methods

Construction of the landslide database related to the Kumamoto earthquake was based on visual interpretation of high-resolution optical ortho-images before and after the earthquake. Aerial photographs from Asia Air Survey CO., LTD. (http://www.ajiko.co.jp/article/detail/ID56JI45Y2D) of very high-resolution and field photos from Kiyota Laboratory in the University of Tokyo (Geo-Disaster Mitigation Engineering, http://www.gdm.iis.u-tokyo.ac.jp/index_e.html) were used to validate this interpretation and thus improve the quality of the database. Pre-earthquake remote sensing images were mainly from the Google Earth (GE) platform, which have the advantages of high-quality, high-resolution, and less cloudy coverage. In addition, the images were acquired within 2 years before the earthquake and cover the entire earthquake-affected area. There are two main sources of remote sensing images after the earthquake: (a) GE platform; (b) GF1, GF2, and ZY3 images from China Centre for Resources Satellite Data and Application (CRESDA) (Fig. 2). Several weeks after the earthquake, the GE platform released a series of satellite images shot soon after the quake from a few commercial companies, such as DigitalGlobe and Astrium. The resolution of these images is pretty satisfactory. A part of the images was acquired on April 15, 2016, which were between the Mj6.5 (Mw6.2) foreshock and the Mj7.3 (Mw7.0) mainshock while several images were taken between April 16 and 20, 2016, i.e., after the Mj7.3 mainshock (Fig. 2). The images of the two periods covered most of the earthquake-affected area, respectively. The satellite images from CRESDA include three types, i.e., GF1, GF2, and ZY3 (Table 1). The coverage of the images used in this study is shown in Fig. 2 with supplements from GE platform. In addition, Sentinel-2 images (https://scihub.copernicus.eu/dhus/#/home) and Landsat-8 ETM+ images (https://earthexplorer.usgs.gov/) freely accessed were also supplements for interpretation coseismic landslides in this study. Finally, we obtained the high-resolution satellite images before and after the earthquake covering the earthquake-affected area. It should be noted that there are quite a few sources of post-quake satellite images and often multiple-source images in an area. We selected images of higher quality and shorter time after the earthquake. We preferred the images from GE platform, but if there were no GE images or the images covered by clouds in some areas, we would consider the satellite images from CRESDA.

Although these satellite images have high resolutions and a high-quality landslide inventory can be anticipated to be derived, validation based on field investigations or very high-resolution aerial photos could further improve the quality of the inventory. In this study, the open accessed data for validating the inventory of landslides triggered by the Kumamoto earthquake include very high-resolution aerial photos covering part of the affected areas released by Asia Air Survey CO., LTD. (http://www.ajiko.co.jp/article/detail/ID56JI45Y2D) and field survey route and photos from Kiyota Laboratory in the University of Tokyo (Geo-Disaster Mitigation Engineering, http://www.gdm.iis.u-tokyo.ac.jp/index_e.html). These allow us to construct a detailed and complete landslide inventory related to the Kumamoto earthquake. Furthermore, we have accumulated abundant experiences in landslide interpretation and detection to major earthquakes of recent years (Xu et al. 2013; Xu et al. 2014b, c, d; Xu et al. 2015a; Tian et al. 2016). We also complied the principles and criteria (Harp et al. 2011; Xu 2015) strictly for landslide mapping to ensure the objectivity and integrity of the resultant database. Generally, the landslide source area is difficult to distinguish accurately from the whole landslide area because the lower boundary of the source area of a landslide is often invisible. Similar to previous studies (Liao and Lee 2000; Harp et al. 2011; Gorum et al. 2014; Xu et al. 2014d; Xu et al. 2015a; Gnyawali et al. 2016), the whole area of a coseismic landslide is delineated as a polygon to represent the landslide itself, no source area being identified. In the subsequent statistics on the relationships between landslide density and topography, geology, and earthquake parameters, we follow this principle.

We compared the high-resolution satellite images and very high-resolution aerial photographs in two areas affected by the Kumamoto quake (Figs. 3 and 4). Figure 3 presents three pieces of satellite images acquired on December 18, 2015 (Fig. 3a), April 15, 2016 (Fig. 3b), and April 19, 2016 (Fig. 3c) and a piece of aerial photograph on April 29, 2016 (Fig. 3d) in an area (32.877°N, 131.044°E) without landslide occurrence before the shock but affected by many coseismic landslides. The comparison between Fig. 3a and Fig. 3b indicates the foreshock did not trigger any landslides in the area. Figure 3c shows significant differences compared to Fig. 3b, which indicates the Mj7.3 mainshock triggered landslides in the area. The coseismic landslides show dark strips different from the surroundings. Figure 3d displays a better representation of coseismic landslides than Fig. 3c. The natural slopes were strongly destroyed by the landslides and fissures also developed there. The arrows in Fig. 3c and d indicate several coseismic landslides. Among them, two landslides in the lower left are not shown because of cloud coverage.

Figure 4 indicates three pieces of satellite imagery of December 18, 2015 (Fig. 4a), April 15, 2016 (Fig. 4b), and April 19, 2016 (Fig. 4c) and a piece of aerial photograph of April 29, 2016 (Fig. 4d) in an area (32.906°N, 131.09E) affected by landslides before the Kumamoto earthquake and more coseismic landslides during the quake. The dark patches in Fig. 4a and b show the same distribution and shapes, implying the landslides already existed before the Kumamoto earthquake and the Mj 6.5 foreshock did not trigger landslides in the area. The arrows in Fig. 4a and b indicate quite a few pre-earthquake landslides. The post-quake image of Fig. 4c indicates the quake triggered many landslides covering most of the area. Figure. 4d shows a more distinct comparison between coseismic landslides and surroundings (green vegetation). The arrows in Fig. 4c and d identify several small areas without coseismic landslides. From the comparisons of pre- and post-earthquake images throughout the affected area, it can be concluded the foreshock almost did not trigger landslides and the massive coseismic landslides were triggered by the Mj 7.3 mainshock. The comparison between satellite images and aerial photographs suggests the satellite images permit to identify coseismic landslides to the identical effect as the aerial photographs.

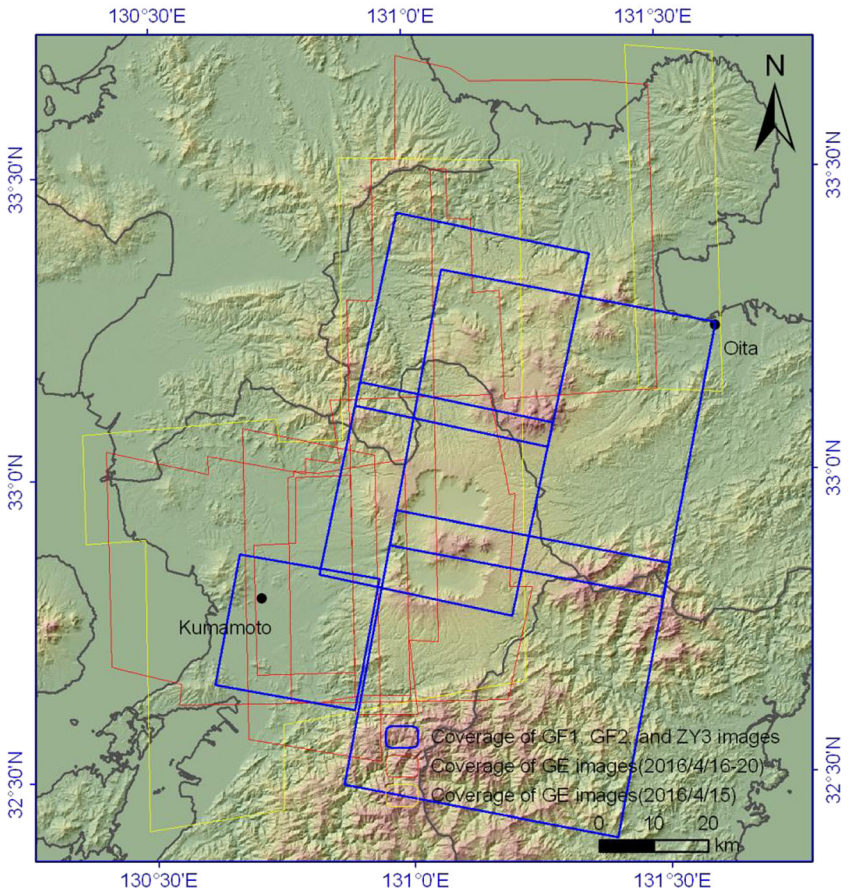

Fig. 2 Coverage of post-earthquake satellite images from GE platform and China Centre for Resources Satellite Data and Application (CRESDA). The hillshade background is derived from SRTM DEM downloaded from USGS EarthExplorer (https://earthexplorer.usgs.gov/). The figure is derived from ArcGIS 9.2 platform (http://www.esrichina.com.cn/softwareproduct/ArcGIS)

Figures 5 and 6 show two large landslides in three-dimensional view from field photos and satellite images. The landslides can be recognized by highlights of strips different from the surroundings. In addition, some of the detailed characteristics can also be observed, such as the sliding direction, damaged vegetation on landslide bodies, destroyed houses, and buried roads. These features enable us to construct an earthquake-triggered landslide database based on the satellite images. Figure 5 shows the largest coseismic landslide (32.886°N, 130.983°E) that buried the Aso Bridge, which is about 168,000 m^2 in area and 2.5 million m^3 in volume. The landslide overwhelmed the Bungo highway (Route 57) and destroyed the Aso Bridge across the river gorge, and at least resulted in one death (NZSEE 2016). Figure 6 shows a landslide (32.877°N, 131.016°E) which seriously destroyed some houses in a hot spring resort and killed two people (Kayen et al. 2016), which is about 13,000 m^2 in area and 0.1 million m^3 in volume.

Landslide inventory and analysis of control factors

Landslide inventory

We delineated 3467 individual landslides triggered by this event (Fig. 7), most of which are shallow, disrupted failures with a few flow-type slides and large rock and soil avalanches (Dai et al. 2016; Dang et al. 2016). The total occupation area of these landslides is about 6.9 km^2. Based on the correlation between landslide area and volume ($V = 1.3147 \times A^{1.2085}$) from Xu et al. (Xu et al. 2016b),

Table 1 Satellite images of GF1, GF2, and ZY3 from CRESDA used in this work

Date	Type	Center location	Spectral information	Resolution
April 17, 2016	GF2	130.8°E, 32.7°N	Pan, MS	1 m, 4 m
April 19, 2016	GF1	131.1°E, 33.0°N	Pan, MS	2 m, 8 m
April 19, 2016	GF1	131.1°E, 33.2°N	Pan, MS	2 m, 8 m
April 20, 2016	ZY3	131.2°E, 32.7°N	Pan, MS	2 m, 6 m
April 20, 2016	ZY3	131.3°E, 33.1°N	Pan, MS	2 m, 6 m

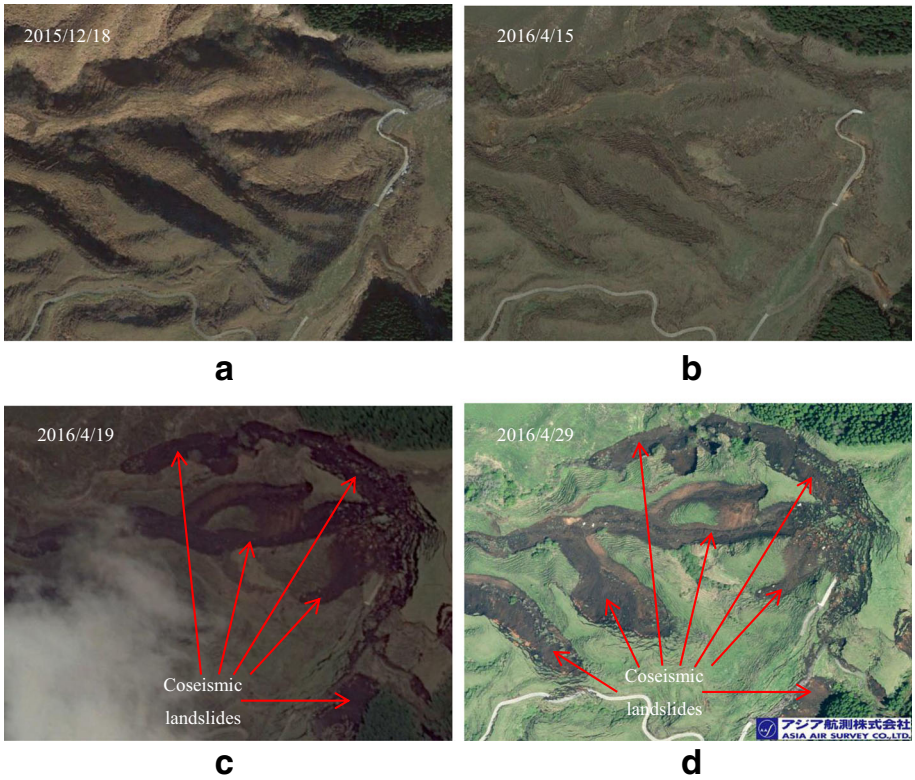

Fig. 3 Ortho satellite images and aerial photograph of an area (32.877°N, 131.044°E, 370 × 290 m) showing landslides triggered by the Kumamoto earthquake. The images were shot on 2015/12/18 (**a**), 2016/4/15 (**b**), 2016/4/19 (**c**), and 2016/4/29 (**d**), respectively. The satellite images (**a**), (**b**), and (**c**) are from GE platform. The image (**d**) from Asia Air Survey CO., LTD. (http://www.ajiko.co.jp/article/detail/ID56JI45Y2D). Up is north

the total volume is estimated to be about 60 million m^3. Of them, 95 landslides are of area larger than 10,000 m^2, 1273 of 1000–10,000 m ^{2}, 1812 of 100–1000 m^2, and the rest 287 landslides are less than 100 m^2 in size. In spatial distribution, 3460 landslides fall in an elliptical area about 6000 km^2, with a NE-SW directed 120-km-long long axis and a 60-km-long NW-SE trending short axis (Fig. 7). Seven landslides are located outside this elliptical area; four pieces north to this area and other three pieces in southwest. The seven landslides are far away from the earthquake epicenter, so not considered in the following analysis on correlations between coseismic landslides and controlling parameters. Because they occurred on the slopes with the critical state of instability, thus would lead to failure under slight perturbations. Such a situation is common in earthquake events (Alfaro et al. 2012; Xu et al. 2014d). It is helpful for analysis on spatial distributions of coseismic landslides more objectively excluding such landslides far distant from earthquake sources.

For the Kumamoto event, the direction of the long axis of the landslide distribution is consistent with the spread direction of the earthquake sequence, implying the way of seismic energy release and surface rupture might control the spatial distribution of the coseismic landslides. While it is different from the common cases that coseismic landslides are symmetrically distributed on either side of the causative strike-slip faults (Gorum et al. 2014; Xu and Xu 2014), instead exhibiting a strong spatially non-uniform pattern. Most of the landslides by this shock (about 2900 pieces, accounting for about 83.8% of the total) occurred in the Aso volcano area about 500 km^2 in size (Fig. 7). The northeast part of the elliptical area has less and sparser landslides, perhaps the Aso volcano stopped the propagation of seismic waves to the northeast. However, some coseismic landslides are concentrated in several areas in the northeast of the epicenter. The affected area northwest to the earthquake sequence is larger than that in the southeast. The possible reason is that the seismogenic fault has a normal component dipping to the northwest, thus majority of the projection area of the rupture surface is located northwest to the seismogenic fault (Fig. 7a).

Factors controlling earthquake-triggered landslides

Earthquake-triggered landslides are mainly controlled by seismic, topographic, and geologic factors. In this section, we analyzed the effects of these controlling factors on the spatial distribution of landslides triggered by the Kumamoto earthquake. Seismic intensity and peak ground acceleration (PGA) were selected as two seismic factors; elevation, slope angle, and slope aspect as three topographic factors; and lithology as a geologic factor. With reference to previous studies (Wang et al. 2007; Xu et al. 2014b, d), landslide number density (LND) and landslide area percentage (LAP) were used as two landslide abundance proxies to measure the spatial pattern of the coseismic landslides related to the Kumamoto earthquake in each controlling parameter. LND represents the landslide number per one square kilometer in unit "km^{-2}" and LAP means the percentage of the area affected by the landslides in unit "%."In the elliptical study area, the total area

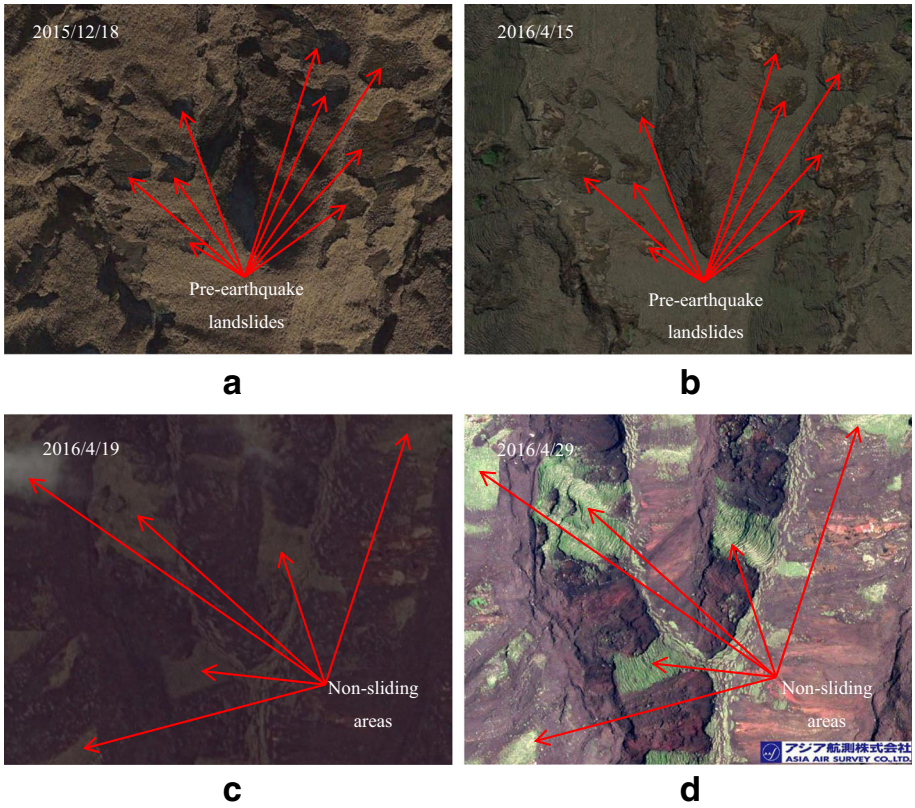

Fig. 4 Ortho satellite images and aerial photograph of an area (32.906°N, 131.09°E, 300 × 250 m) showing landslides triggered by the Kumamoto earthquake. The images were shot on 2015/12/18 (**a**), 2016/4/15 (**b**), 2016/4/19 (**c**), and 2016/4/29 (**d**), respectively. The satellite images (**a**), (**b**), and (**c**) are from GE platform. The image (**d**) from Asia Air Survey CO., LTD. (http://www.ajiko.co.jp/article/detail/ID56JI45Y2D). Up is north

of the 3460 coseismic landslides is about 6.92 km^2 and the average area of the landslides is about 2000 m^2. Therefore, the LND and LAP of the area are 3460/5972.6 km^2 = 0.58 km^{-2} and 6.92 km^2 / 5972.6 km^2 = 0.116%, respectively.

Figure 8 shows the relationships between landslide abundance (including LND and LAP) and elevation, slope angle, and slope aspect. The elevation data is derived from SRTM DEM (1 arc) with ~ 30 m resolution (https://earthexplorer.usgs.gov/). We resampled SRTM DEM into a 5 m–resolution DEM by the least square interpolation method. The study area is dominated by plain, gentle slopes, and volcanic landscape with low elevation and moderate topographic relief and hillslope steepness. The elevation of study area ranges from 0 to 1769 m, mostly lower than 1000 m. The total area with elevation less than 1000 m is about 5661 km^2, accounting for 95% of the entire area. Figure 8a indicates that the elevation interval of 600–800 m registers the largest landslide number of 928 pieces, with a total area 1.7 km^2. The elevation range of the maximum total landslide area, which is 2.15 km^2, is 800–1000 m,

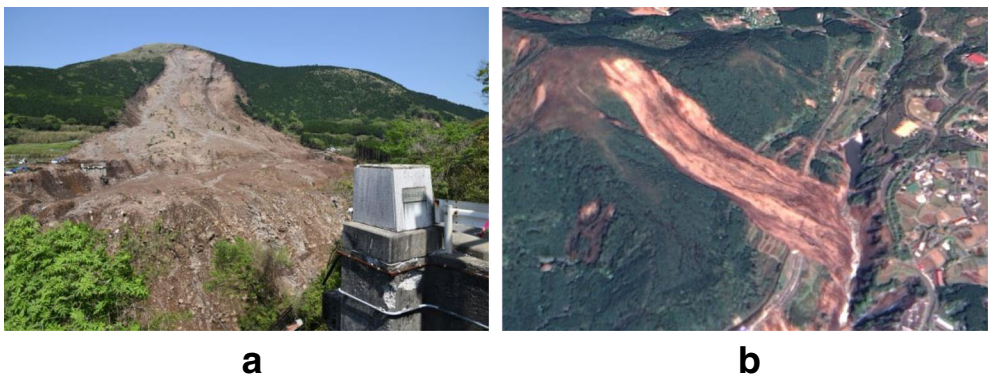

Fig. 5 Landslide at Aso Bridge (32.886°N, 130.983°E). **a** Field photo taken on April 30, 2016 by Shinji Toda, view to west. **b** 2-m resolution ZY3 image shot on April 20, 2016 in three-dimensional view, view to north

Fig. 6 Landslide at Hot Spring Resort (32.877°N, 131.016°E). **a** Field photo taken on April 23, 2016 by Kiyota Laboratory (Geo-Disaster Mitigation Engineering, http://www.gdm.iis.u-tokyo.ac.jp/index_e.html), view to NWW. **b** Very high-resolution satellite image from DigitalGlobe on GE platform shot on April 19, 2016 in three-dimensional view, view to NWW

corresponding to 858 coseismic landslides. This indicates the landslides in the elevation 800–1000 m have a larger coverage area. From the results of landslide abundance in each elevation class, it can be noted that the elevation range of 1000–1200 m has the largest LAP and LND, i.e., 2.22 km^{-2} and 0.47%, respectively. The LAP and LND generally decrease with the elevation far from 1000 to 1200 m. We infer that the impact of elevation on coseismic landslides is perhaps controlled by other factors, such as slope angle, aspect, and precipitation. Figure 8b shows the class area, LND, and LAP in each class of slope angle. The range of the slope angle of the study area is from 0° to 78.7°. The study area is dominated by gentle slopes. The coverage area of slope gradually

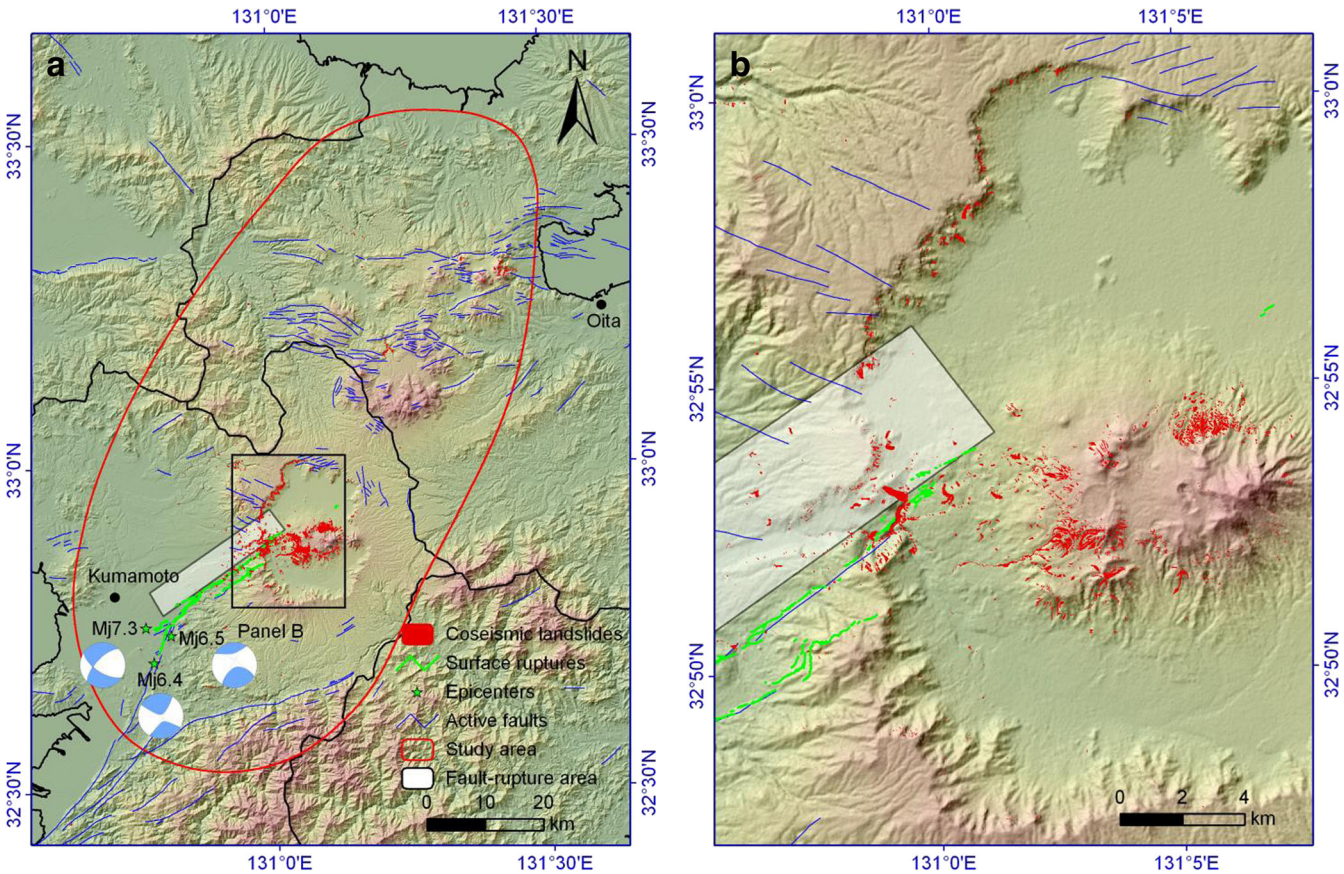

Fig. 7 Distribution of landslides triggered by the Kumamoto earthquake. **a** Inventory map. **b** the enlarged area of the black rectangle on panel **a**. The hillshade background is derived from SRTM DEM downloaded from USGS EarthExplorer (https://earthexplorer.usgs.gov/). The figure is derived from ArcGIS 9.2 platform (http://www.esrichina.com.cn/softwareproduct/ArcGIS). The earthquake focal mechanism beach balls are from USGS Earthquake Hazards Program (https://earthquake.usgs.gov/earthquakes/browse/significant.php)

decreases with the increasing slope angle. The average angle of the study area is 14°. Most of the area is covered by slopes with angle ≤ 30°, about 5520 km^2, occupying 92.5% of the total study area. The tendencies of LND and LAP with slope angle are similar. Landslide abundance increases with increasing slope angle. The angle range of 40°–78.7° registers the highest landslide abundance, with LND and LAP 5.5 km^{-2} and 0.82%, respectively. This tendency has also been observed in many other earthquakes. Because the effective gravity of steep slopes is larger than gentle slopes, thus resulting in higher susceptibility of landslides and more failures during earthquakes (Xu et al. 2014c, d). In slope aspect (facing direction), the study area was divided into nine classes, i.e., flat, north, northeast, east, southeast, south, southwest, west, and northwest. Figure 8c shows the relationships between slope aspect and class area, LND and LAP. The area of each class occupies a similar area except the flat class. Previous studies (Xu et al. 2014d; Shen et al. 2016) show slope aspect can influence the landslide occurrence by the propagation direction of seismic waves. Different from other major earthquakes, the coseismic landslides triggered by the 2016 Kumamoto event do not have an obvious relationship with slope aspect. Perhaps because the mechanism of this event is rather complex and the propagation direction of the seismic waves and movement direction of the blocks are rather random.

According to the 1:200,000 geological map of Japan (Geological Survey of Japan 2012), we divided the study area into 58 lithologic classes. Of them, 32 lithology classes have no landslide and 13 classes registered only 1–9 landslides with LAP values less than 0.1 km^{-2}. These classes were not taken into account because the lower coseismic landslide susceptibility and small landslide samples might result in high errors. Finally, we calculated the landslide number, landslide area, LND, and LAP in the remaining 13 classes of the lithology (Table 2 and Fig. 9). Results show that the strata of Q_3-H*vb* and Q_3-H*vf* registered the largest landslide number, which are 922 and 805 pieces, respectively. The strata of Q_3-H*vb* and Q_3-H*vf* register the two largest landslide areas, LND and LAP, which are 2.446 and 1.814 km^2, 8.418 and 15.07 km^{-2}, and 2.233 and

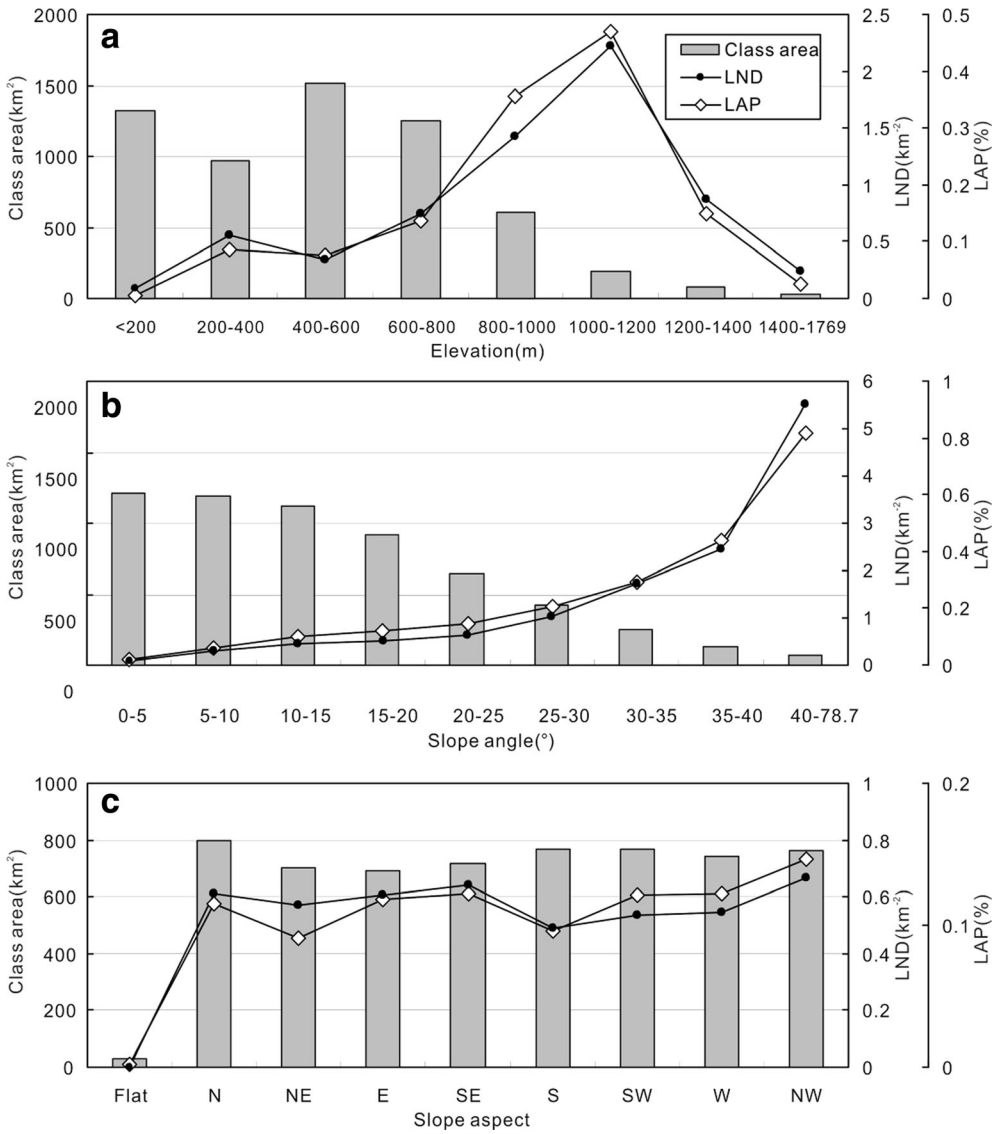

Fig. 8 Relationships between the coseismic landslides and topography. **a** Elevation. **b** Slope angle. **c** Slope aspect

Table 2 Statistics of landslides triggered in different strata

Code	Descriptions	CA	LN	LA	LND	LAP
H*vb*	Holocene non-alkaline mafic volcanic rocks	69.42	276	0.528	3.976	0.761
H*sr*	Late Pleistocene to Holocene marine and non-marine sediments	759	142	0.129	0.187	0.017
Q_3-H*vb*	Late Pleistocene to Holocene non-alkaline mafic volcanic rocks	109.53	**922**	**2.446**	**8.418**	**2.233**
Q_3-H*vf*	Late Pleistocene to Holocene non-alkaline felsic volcanic rocks	50.56	762	**1.814**	**15.07**	**3.588**
Q_3-H*vp*	Late Pleistocene to Holocene non-alkaline pyroclastic flow volcanic rocks	**1315.2**	74	0.065	0.056	0.005
Q_3*tl*	Late Pleistocene lower terrace	74.57	10	0.045	0.134	0.06
Q_2*vb*	Middle Pleistocene non-alkaline mafic volcanic rocks	566.47	**805**	1.329	1.421	0.235
Q_2*vp*	Middle Pleistocene non-alkaline pyroclastic flow volcanic rocks	350.21	351	0.445	1.002	0.127
Q_1*vp*	Early Pleistocene non-alkaline pyroclastic flow volcanic rocks	331.56	19	0.018	0.057	0.005
N_3*vb*	Late Miocene to Pliocene non-alkaline mafic volcanic rocks	**967.18**	39	0.023	0.04	0.002
K_2*sn*	Late Cretaceous non-marine sediments	73.53	9	0.008	0.122	0.011
PZ*fp*	Paleozoic plutonic rocks	7.57	1	0.002	0.132	0.03
M_7*tux*	Abukuma metamorphic rocks (gneiss and schist)	71.49	10	0.008	0.14	0.012

Two bold numbers in each column represent the largest values in the column

CA area of each stratigraphic classification, *LN* landslide number, *LA* landslide area, *LND* landslide number density, *LAP* landslide area percentage

3.588%, respectively. The stratum of Q_3-H*vf* is the most susceptible, followed by Q_3-H*vb*, which indicates the strata have strong effect on the occurrence of the coseismic landslides.

Earthquake intensity and PGA characterize seismic energy and the destroy degree of earthquakes. The earthquake intensity map and PGA map of the Kumamoto earthquake (Fig. 10) were downloaded from US Geological Survey (US Geological Survey 2016). In general, both the seismic intensity and the PGA related to the Kumamoto earthquake show a predominant SW-NE distribution, which is consistent with the direction of the seismogenic structure and the distribution of aftershocks. The statistics of landslides and seismic intensity is shown in Fig. 11a, which indicates that the landslide number is significantly larger in the places of intensity VIII and VIII+ in the Modified Mercalli Intensity scale that is equivalent to intensity 5-upper in the Japan Meteorological Agency (JMA) Intensity scale. This means that the seismic intensity threshold to induce landslides is approximately VIII. The area with seismic intensity less than VIII has much lower landslide abundances, which are less than 0.5 km^{-2} and 0.05% for LND and LAP, respectively. In the areas of seismic intensity VIII and VIII+, the values of LND and LAP suddenly rise to 4 km^{-2} and 1%, respectively, implying the coseismic landslides are strongly controlled by seismic intensity. The relationship between peak ground acceleration (PGA) and landslide occurrence (Fig. 11b) also indicates that LND and LAP generally increase with growing PGA, except for the area of PGA 0.7 g. Perhaps because the area of PGA 0.7 g has low slope angles and is relatively less prone to landslide occurrence. This area has a very low landslide abundance though it suffered strong ground shaking during the earthquake. In other areas, i.e., PGA 0.1–0.6 g, LND and LAP generally increase with the increasing PGA. The largest values of LND and LAP are in the area of PGA 0.6 g, which are 3.41 km^{-2} and 0.61%, respectively. Collectively, the coseismic landslides triggered by the Kumamoto earthquake are strongly controlled by seismic intensity and PGA. The landslide abundance generally increases with growing PGA or seismic intensity. It should be noted that besides of seismic

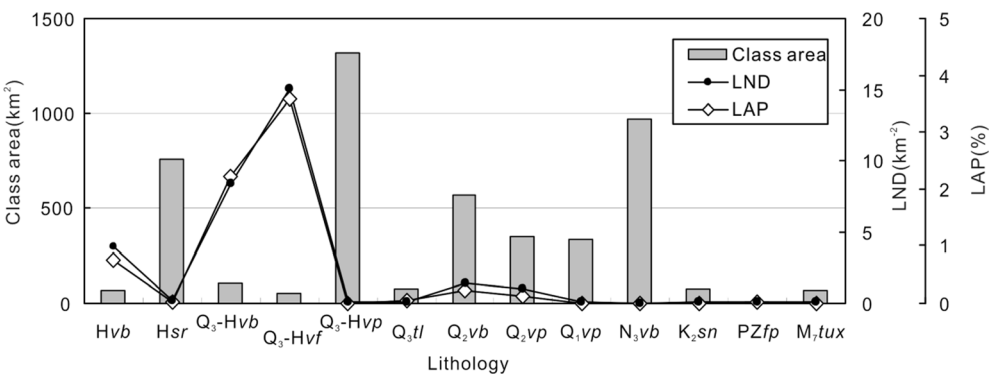

Fig. 9 Relationship between lithology and coseismic landslides

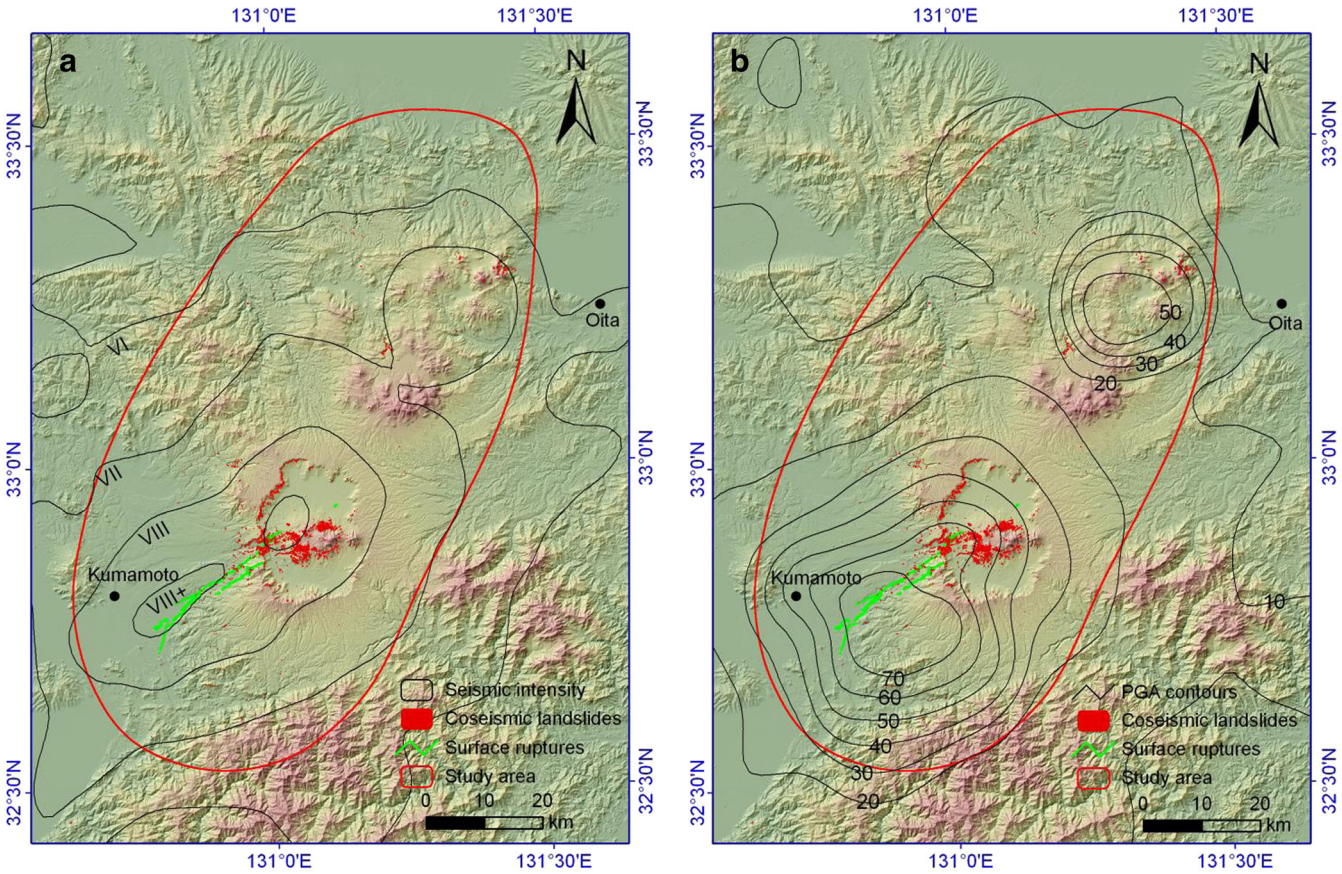

Fig. 10 Distribution maps of seismic intensity (**a**) and PGA/gal (**b**) related to the Kumamoto earthquake

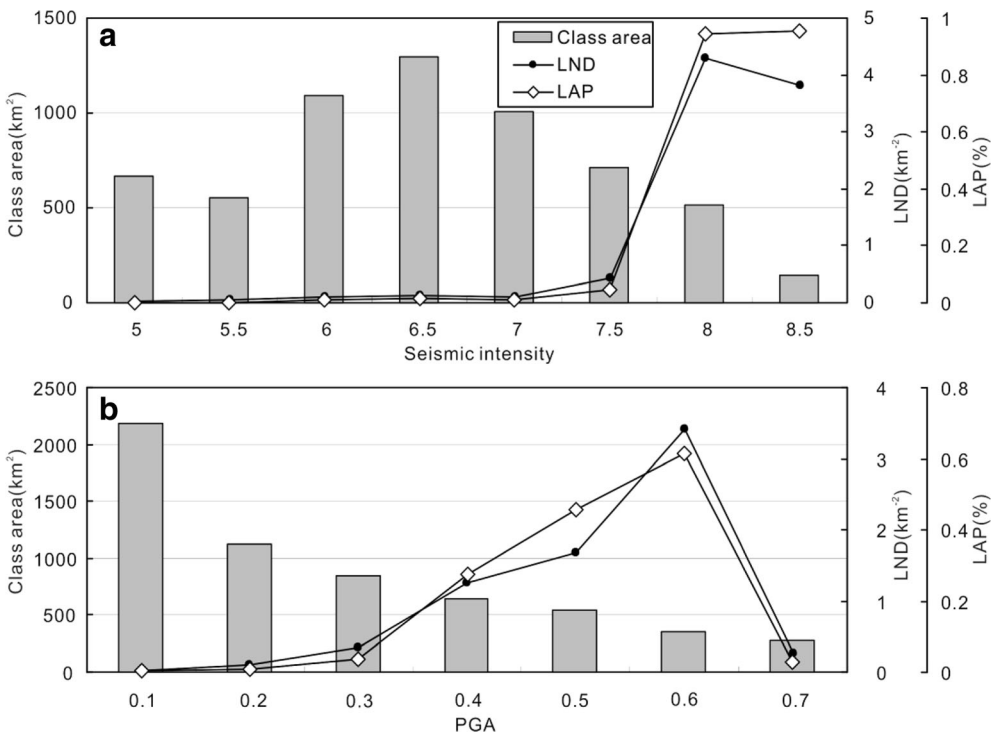

Fig. 11 Relationships between coseismic landslides and earthquake parameters. **a** Seismic intensity. **b** PGA

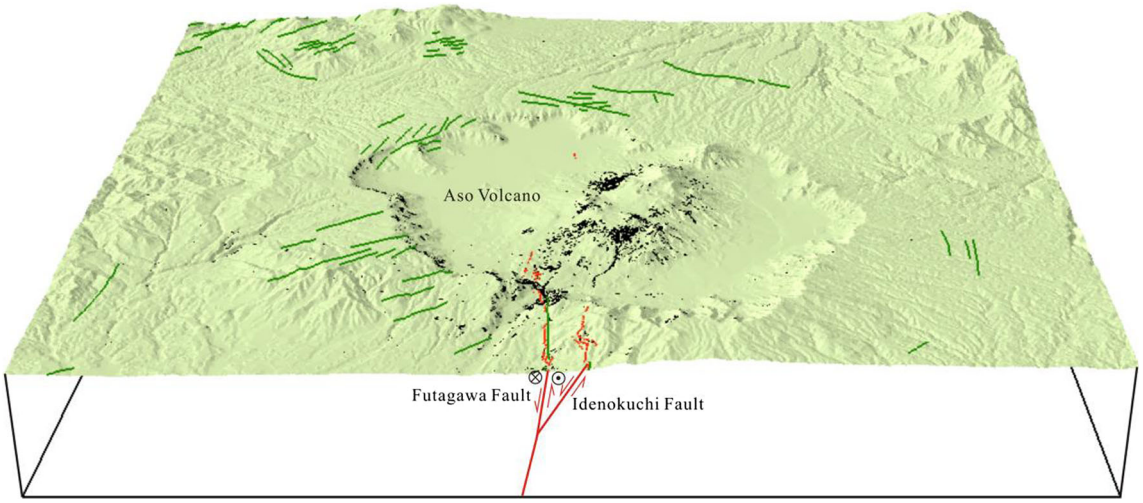

Fig. 12 Three-dimensional view of coseismic landslides and seismogenic faults in Aso volcano area. Green lines on the surface are active faults modified from Active Fault Research Group (Active Fault Research Group 1991) and Kato et al. (Kato et al. 2016). Red lines on the surface and cross section are coseismic surface ruptures and seismogenic faults, respectively. View to northeast. The hillshade background is derived from SRTM DEM downloaded from USGS EarthExplorer (https://earthexplorer.usgs.gov/). The figure is derived from ArcGIS 9.2 platform (http://www.esrichina.com.cn/softwareproduct/ArcGIS)

intensity and PGA, other earthquake parameters may also influence the occurrence of coseismic landslides, such as peak ground velocity (PGV), rupture distance, fault categories, Arias intensity, shear wave velocity at top 30 m Vs_{30}, as well as Newmark

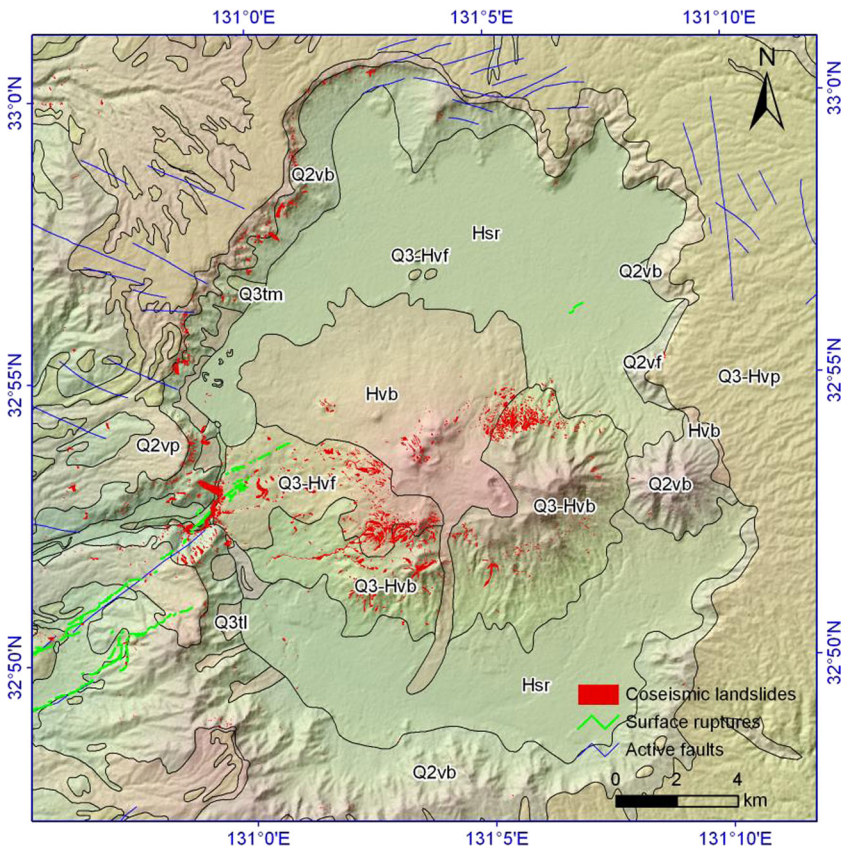

Fig. 13 Geologic map (Geological Survey of Japan 2012) of the Aso volcano area and distributions of active faults, coseismic surface ruptures, and coseismic landslides related to the Kumamoto earthquake. The hillshade background is derived from SRTM DEM downloaded from USGS EarthExplorer (https://earthexplorer.usgs.gov/). The figure is derived from ArcGIS 9.2 platform (http://www.esrichina.com.cn/softwareproduct/ArcGIS)

displacement derived from the above seismic parameters (Jibson 2011; Du and Wang 2014; Du and Wang 2016). It is worth carrying out further study on these relationships between coseismic landslides and seismic parameters in the future.

The most impressive characteristic of the landslides triggered by the Kumamoto earthquake is their high concentration around the Aso volcano area. Figure 12 shows the three-dimensional view of the structural model and the distribution of coseismic landslides in the study area. Two northeast-trending subparallel surface ruptures, i.e., the Futagawa fault dominated by right-lateral strike-slip with a normal fault component dipping to northwest and the Idenokuchi fault with dominant normal fault dipping to northwest (Toda et al. 2016). The terminal of the ruptures is nearby the Aso volcano. The high concentration of coseismic landslides in the area is considered to be associated with joint control by the seismogenic fault, topography, and geologic conditions. The terminals of seismogenic faults are usually the localities with strong stress releasing and large deformation, coupled with the Aso volcano stopping the northeastward spread of the earthquake rupture. The topography of inner slopes around the Aso volcano is the steepest, thus resulted in high concentration of coseismic landslides in the area. Geologically, several kinds of volcanic rock layers (i.e., Q_3-H*vb*, Q_3-H*vf*, Q_2*vb*, and Q_2*vp*) have low strengths and thus are prone to failure under strong earthquake shaking and deformation. Figure 13 clearly shows the effects of Middle Pleistocene, Late Pleistocene, and Holocene volcanic rocks on the occurrence of the coseismic landslides. In the study area, many landslides occurred before the earthquake indicative of the high susceptibility of landslides. We observed a considerable part of coseismic landslides occurred in the areas between the Futagawa fault and Idenokuchi fault and the hanging wall of the Idenokuchi fault. Such a phenomenon was clearly observed at the inner slopes around the Aso volcano. The northwest part of the ring distribution slopes around the Aso volcano registered more coseismic landslides than other parts. This is perhaps because the northwest part is located on the hanging wall of the Futagawa fault (Fig. 12), which is the fault rupture projection area of the Kumamoto earthquake where developed high incidence and severe coseismic landslides (Tatard and Grasso 2013).

Although the magnitude of the largest foreshock of the Kumamoto quake sequence is as large as Mj 6.5, and a moderate earthquake should have the ability to trigger coseismic landslides (Keefer 1984; Xu et al. 2014a; Xu et al. 2015a; Tian et al. 2016), little landslides were triggered by this foreshock (c.f., Figs. 3 and 4). Almost all the coseismic landslides were triggered by the Mj 7.3 mainshock. This suggests the correlations between earthquake magnitude and overall incidence and severity of landsliding is nonlinear. The occurrence of massive coseismic landslides needs a threshold of earthquake magnitude between Mj 6.5 and Mj 7.3 with a similar focal mechanism to the Kumamoto earthquake in the area. The spatial patterns of coseismic landslides triggered by earthquakes occurred on different types of seismogenic faults are proved to be different. Landslides triggered by reverse-fault earthquakes are more likely to be located at the hanging wall of the fault, and densely distributed along the seismogenic fault (Wang et al. 2003; Owen et al. 2008; Xu et al. 2014d; Xu et al. 2015a). Strike-slip fault earthquakes usually trigger landslides with a symmetrical and concentrating distribution along the fault (Gorum et al. 2014; Xu and Xu 2014). However, case studies of coseismic landslides triggered by earthquakes on normal faults are rather rare. The Kumamoto case provides us a chance to understand the spatial pattern of landslides induced by an earthquake generated by a fault with a normal fault component. The mechanism of the Kumamoto earthquake is dominated by right-lateral strike-slip with a normal fault component dipping to the northwest. Results show the coseismic landslides have a highly non-uniform pattern, which is very different from coseismic landslides triggered by reverse faults or purely strike-slip faults. Most of the landslides triggered by the Kumamoto earthquake occurred around the northeast terminal of the seismogenic fault. The normal fault component appears to play an important role in the spatial pattern of the coseismic landslides. Most of the landslides occurred on the hanging wall of the Idenokuchi fault. Such an effect by the normal fault component was clearly seen on the inner slopes around the Aso volcano. The northwest part of the rounded slopes registers much more coseismic landslides than other areas with similar topographic and geologic conditions.

Conclusions

Based on high-resolution (0.5–2 m) optical satellite images before and after the event, with the validation using ortho-aerial photographs with very high-resolution (better than 0.5 m) and oblique field photos, we delineated 3467 individual coseismic landslides throughout the affected area triggered by the 2016 Kumamoto, Japan Mj7.3 earthquake. The resultant database is much more detailed than other ones released by previous work immediately after the earthquake. The total occupation area of these landslides is about 6.9 km^2. Of them, 3460 landslides are distributed in an elliptical area about 6000 km^2, with a NE-SW directed 120-km-long long axis and a 60-km-long NW-SE short axis. Most of the landslides are shallow, disrupted failures, with a few flow-type landslides and rock and soil avalanches. These landslides show a strong spatially non-uniform pattern; most of which (about 2900 pieces) occurred in the Aso volcano area about 500 km^2. The Mj 6.5 foreshock triggered little landslides, almost all the coseismic landslides were attributed to by the Mj 7.3 mainshock. The high concentration of the coseismic landslides in this area is considered to be jointly controlled by the seismic shaking, seismogenic fault, topography, and geologic conditions. The normal fault component of the seismogenic fault might have a strong effect on the spatial pattern of the coseismic landslides. Most of the landslides are concentrated on the hanging wall of the Idenokuchi fault. The correlations between the coseismic landslides and several condition factors were analyzed. Results show the places of elevation 1000–1200 m, strata of Q_3-H*vf*, seismic intensity VIII and VIII+, and peak ground acceleration (PGA) 0.4–0.6 g account for the largest landslide abundance. This paper presents a case study of inventory preparation and spatial pattern of landslides triggered by a strike-slip fault with a normal component that generated earthquakes in a volcano area, and thus is helpful for research of coseismic landslides in areas with similar topographic and geologic conditions.

Acknowledgments

We thank Aitaro Kato for his help in collecting data used in this study. We are grateful to the anonymous reviewers for their suggestive comments.

Funding information

This study was supported by the major international (regional) joint research project (41661144037) from the National Natural Science Foundation of China (NSFC) and the International Centre for Integrated Mountain Development (ICIMOD) and the National Key Research and Development Program of China (Project No. 2017YFB0504104).

References

Active Fault Research Group (1991) Active faults in Japan: sheet maps and inventories (revised edition). University of Tokyo Press, Tokyo 437 pp

Alfaro P, Delgado J, García-Tortosa FJ, Lenti L, López JA, López-Casado C, Martino S (2012) Widespread landslides induced by the Mw 5.1 earthquake of 11 May 2011 in Lorca, SE Spain. Eng Geol 137-138:40–52. https://doi.org/10.1016/j.enggeo.2012.04.002

Amante C, Eakins BW (2009). ETOPO1 1 arc-minute global relief model: procedures, data sources and analysis, US Department of Commerce, National Oceanic and Atmospheric Administration, National Environmental Satellite, Data, and Information Service, National Geophysical Data Center, Marine Geology and Geophysics Division Colorado. https://www.ngdc.noaa.gov/mgg/global/relief/ETOPO1/docs/ETOPO1.pdf

Asano K, Iwata T (2016) Source rupture processes of the foreshock and mainshock in the 2016 Kumamoto earthquake sequence estimated from the kinematic waveform inversion of strong motion data. Earth Planets Space 68(1):147. https://doi.org/10.1186/s40623-016-0519-9

British Geological Survey, Earthquakes without Frontiers, Durham University (2015) 2015 Nepal earthquakes mapped landslide intensity (Revision 4.0–19 June 2015). https://data.hdx.rwlabs.org/group/nepal-earthquake

Dai Z, Wang F, Huang Y, Song K, Iio A (2016) SPH-based numerical modeling for the post-failure behavior of the landslides triggered by the 2016 Kumamoto earthquake. Soc Geogr Discuss 3(1):24. https://doi.org/10.1186/s40677-016-0058-5

Dang K, Sassa K, Fukuoka H, Sakai N, Sato Y, Takara K, Quang LH, Loi DH, Van Tien P, Ha ND (2016) Mechanism of two rapid and long-runout landslides in the 16 April 2016 Kumamoto earthquake using a ring-shear apparatus and computer simulation (LS-RAPID). Landslides 13(6):1525–1534. https://doi.org/10.1007/s10346-016-0748-9

Du W, Wang G (2014) Fully probabilistic seismic displacement analysis of spatially distributed slopes using spatially correlated vector intensity measures. Earthq Eng Struct Dyn 43(5):661–679. https://doi.org/10.1002/eqe.2365

Du W, Wang G (2016) A one-step Newmark displacement model for probabilistic seismic slope displacement hazard analysis. Eng Geol 205:12–23. https://doi.org/10.1016/j.enggeo.2016.02.011

Fujiwara S, Yarai H, Kobayashi T, Morishita Y, Nakano T, Miyahara B, Nakai H, Miura Y, Ueshiba H, Kakiage Y, Une H (2016) Small-displacement linear surface ruptures of the 2016 Kumamoto earthquake sequence detected by ALOS-2 SAR interferometry. Earth Planets Space 68(1):160. https://doi.org/10.1186/s40623-016-0534-x

Furumura T (2016) Destructive near-fault strong ground motion from the 2016 Kumamoto prefecture, Japan, M7.3 earthquake. Landslides 13(6):1519–1524. https://doi.org/10.1007/s10346-016-0760-0

Geological Survey of Japan (2012). AIST (ed.), Seamless digital geological map of Japan 1: 200,000. Jul 3, 2012 version. Research Information Database DB084, Geological Survey of Japan, National Institute of Advanced Industrial Science and Technology. https://gbank.gsj.jp/seamless/

Gnyawali KR, Maka S, Adhikari BR, Chamlagain D, Duwal S, Dhungana AR (2016). Spatial implications of earthquake induced landslides triggered by the April 25 Gorkha Earthquake Mw 7.8: preliminary analysis and findings. International Conference on Earthquake Engineering and Post Disastor Reconstruction Planning 24–26 April, 2016, Bhaktapur, Nepal: 50–58

Goda K, Campbell G, Hulme L, Ismael B, Ke L, Marsh R, Sammonds P, So E, Okumura Y, Kishi N, Koyama M, Yotsui S, Kiyono J, Wu S, Wilkinson S (2016) The 2016 Kumamoto earthquakes: cascading geological hazards and compounding risks. Front Built Environ 2:19

Gorum T, Korup O, van Westen CJ, van der Meijde M, Xu C, van der Meer FD (2014) Why so few? Landslides triggered by the 2002 Denali earthquake, Alaska. Quat Sci Rev 95:80–94. https://doi.org/10.1016/j.quascirev.2014.04.032

Goto H, Tsutsumi H, Toda S, Kumahara Y (2017) Geomorphic features of surface ruptures associated with the 2016 Kumamoto earthquake in and around the downtown of Kumamoto City, and implications on triggered slip along active faults. Earth Planets and Space 69(1):26. https://doi.org/10.1186/s40623-017-0603-9

Harp EL, Jibson RW (1995) Inventory of landslides triggered by the 1994 Northridge, California earthquake. US Geological Survey, http://pubs.usgs.gov/of/1995/ofr-95-0213/plate1.gif; http://geo-nsdi.er.usgs.gov/metadata/open-file/95-213/

Harp EL, Keefer DK, Sato HP, Yagi H (2011) Landslide inventories: the essential part of seismic landslide hazard analyses. Eng Geol 122(1–2):9–21. https://doi.org/10.1016/j.enggeo.2010.06.013

Himematsu Y, Furuya M (2016) Fault source model for the 2016 Kumamoto earthquake sequence based on ALOS-2/PALSAR-2 pixel-offset data: evidence for dynamic slip partitioning (EPSP-D-16-00163). Earth Planets Space 68(1):169. https://doi.org/10.1186/s40623-016-0545-7

Jibson RW (2011) Methods for assessing the stability of slopes during earthquakes—a retrospective. Eng Geol 122(1–2):43–50. https://doi.org/10.1016/j.enggeo.2010.09.017

Kargel JS, Leonard GJ, Shugar DH, Haritashya UK, Bevington A, Fielding EJ, Fujita K, Geertsema M, Miles ES, Steiner J, Anderson E, Bajracharya S, Bawden GW, Breashears DF, Byers A, Collins B, Dhital MR, Donnellan A, Evans TL, Geai ML, Glasscoe MT, Green D, Gurung DR, Heijenk R, Hilborn A, Hudnut K, Huyck C, Immerzeel WW, Jiang L, Jibson R, Kääb A, Khanal NR, Kirschbaum D, Kraaijenbrink PDA, Lamsal D, Liu S, Lv M, McKinney D, Nahirnick NK, Nan Z, Ojha S, Olsenholler J, Painter TH, Pleasants M, Pratima KC, Qi Y, Raup BH, Regmi D, Rounce DR, Sakai A, Shangguan D, Shea JM, Shrestha AB, Shukla A, Stumm D, van der Kooij M, Voss K, Wang X, Weihs B, Wolfe D, Wu L, Yao X, Yoder MR, Young N (2016) Geomorphic and geologic controls of geohazards induced by Nepal's 2015 Gorkha earthquake. Science 351(6269):aac8353

Kato A, Fukuda JI, Nakagawa S, Obara K (2016) Foreshock migration preceding the 2016 Mw 7.0 Kumamoto earthquake, Japan. Geophys Res Lett 43(17):8945–8953. https://doi.org/10.1002/2016GL070079

Kayen R, Dashti S, Kokusho T, Hazarika H, Franke K, Oettle N, Wham B, Calderon JR, Briggs D, Guillies S, Cheng K, Tanoue Y, Takematsu K, Matsumoto D, Morinaga T, Furuichi H, Kitano Y, Tajiri M, Chaudhary B, Nishimura K, Chu C (2016) Geotechnical aspects of the 2016 Mw 6.2, Mw 6.0, and Mw 7.0 Kumamoto earthquakes. Geotechnical Extreme Events Reconnaissance Association, Version 1.0, July 2016. https://pubs.er.usgs.gov/publication/70185571

Keefer DK (1984) Landslides caused by earthquakes. Geol Soc Am Bull 95(4):406–421. https://doi.org/10.1130/0016-7606(1984)95<406:LCBE>2.0.CO;2

Liao HW, Lee CT (2000) Landslides triggered by the Chi-Chi earthquake. Proceedings of the 21st Asian conference on remote sensing, Taipei 1–2:383–388

Matsumoto N, Yoshihiro H, Sawada A (2016) Continuity, segmentation and faulting type of active fault zones of the 2016 Kumamoto earthquake inferred from analyses of a gravity gradient tensor. Earth Planets Space 68(1):167. https://doi.org/10.1186/s40623-016-0541-y

Miyakawa A, Sumita T, Okubo Y, Okuwaki R, Otsubo M, Uesawa S, Yagi Y (2016) Volcanic magma reservoir imaged as a low-density body beneath Aso volcano that terminated the 2016 Kumamoto earthquake rupture. Earth Planets Space 68(1):208. https://doi.org/10.1186/s40623-016-0582-2

Moya L, Yamazaki F, Liu W, Chiba T (2017) Calculation of coseismic displacement from lidar data in the 2016 Kumamoto, Japan, earthquake. Nat Hazards Earth Syst Sci 17(1):143–156. https://doi.org/10.5194/nhess-17-143-2017

Nakata T, Imaizumi T (2002) Digital active fault map of Japan. University of Tokyo Press, Tokyo

NZSEE (2016) Learning from earthquakes mission: Kumamoto earthquake 2016, Japan. New Zealand Society for Earthquake Engineering Inc., http://www.eqclearinghouse.org/2016-04-15-kumamoto/files/2016/04/NZSEE_Kumamoto_Report.pdf

Okumura K (2016). Earthquake geology of the April 14 and 16, 2016 Kumamoto earthquakes, The Kumamoto Earthquake Investigation: a preliminary report, p 6. http://home.hiroshimau.ac.jp/kojiok/kumamoto2016KOreport2.pdf

Owen LA, Kamp U, Khattak GA, Harp EL, Keefer DK, Bauer MA (2008) Landslides triggered by the 8 October 2005 Kashmir earthquake. Geomorphology 94(1–2):1–9. https://doi.org/10.1016/j.geomorph.2007.04.007

Sano Y, Takahata N, Kagoshima T, Shibata T, Onoue T, Zhao D (2016) Groundwater helium anomaly reflects strain change during the 2016 Kumamoto earthquake in Southwest Japan. Sci Rep 6(1):37939. https://doi.org/10.1038/srep37939

Shen L, Xu C, Liu L (2016) Interaction among controlling factors for landslides triggered by the 2008 Wenchuan, China Mw 7.9 earthquake. Front Earth Sci 10(2):264–273

Sugito N, Goto H, Kumahara Y, Tsutsumi H, Nakata T, Kagohara K, Matsuta N, Yoshida H (2016) Surface fault ruptures associated with the 14 April foreshock (Mj 6.5) of the 2016 Kumamoto earthquake sequence, southwest Japan. Earth Planets Space 68(1):170. https://doi.org/10.1186/s40623-016-0547-5

Tatard L, Grasso JR (2013) Controls of earthquake faulting style on near field landslide triggering: the role of coseismic slip. J Geophys Res Solid Earth 118(6):2953–2964

Tian Y, Xu C, Xu X, Chen J (2016) Detailed inventory mapping and spatial analyses to landslides induced by the 2013 Ms 6.6 Minxian earthquake of China. J Earth Sci 27(6):1016–1026. https://doi.org/10.1007/s12583-016-0905-z

Toda S, Kaneda H, Okada S, Ishimura D, Mildon ZK (2016) Slip-partitioned surface ruptures for the Mw 7.0 16 April 2016 Kumamoto, Japan, earthquake. Earth Planets Space 68(1):188. https://doi.org/10.1186/s40623-016-0560-8

Tsuji T, Ishibashi JI, Ishitsuka K, Kamata R (2017) Horizontal sliding of kilometre-scale hot spring area during the 2016 Kumamoto earthquake. Sci Rep 7:42947. https://doi.org/10.1038/srep42947

Uchide T, Horikawa H, Nakai M, Matsushita R, Shigematsu N, Ando R, Imanishi K (2016) The 2016 Kumamoto–Oita earthquake sequence: aftershock seismicity gap and dynamic triggering in volcanic areas. Earth Planets Space 68(1):180. https://doi.org/10.1186/s40623-016-0556-4

US Geological Survey (2016) M 7.0 - 1km E of Kumamoto-shi, Japan. Map Version 8, https://earthquake.usgs.gov/earthquakes/eventpage/us20005iis#executive

Wang WN, Wu HL, Nakamura H, Wu SC, Ouyang S, Yu MF (2003) Mass movements caused by recent tectonic activity: the 1999 Chi-Chi earthquake in central Taiwan. Island Arc 12(4):325–334. https://doi.org/10.1046/j.1440-1738.2003.00400.x

Wang HB, Sassa K, Xu WY (2007) Analysis of a spatial distribution of landslides triggered by the 2004 Chuetsu earthquakes of Niigata prefecture, Japan. Nat Hazards 41(1):43–60. https://doi.org/10.1007/s11069-006-9009-x

Xu C (2015) Preparation of earthquake-triggered landslide inventory maps using remote sensing and GIS technologies: principles and case studies. Geosci Front 6(6):825–836. https://doi.org/10.1016/j.gsf.2014.03.004

Xu C, Xu X (2014) Statistical analysis of landslides caused by the Mw 6.9 Yushu, China, earthquake of April 14, 2010. Nat Hazards 72(2):871–893. https://doi.org/10.1007/s11069-014-1038-2

Xu C, Xu X, Yu G (2013) Landslides triggered by slipping-fault-generated earthquake on a plateau: an example of the 14 April 2010, Ms 7.1, Yushu, China earthquake. Landslides 10(4):421–431. https://doi.org/10.1007/s10346-012-0340-x

Xu C, Xu X, Shen L, Dou S, Wu S, Tian Y, Li X (2014a) Inventory of landslides triggered by the 2014 Ms 6.5 Ludian earthquake and its implications on several earthquake parameters. Seismol Geol 36(4):1186–1203

Xu C, Xu X, Shyu JBH, Zheng W, Min W (2014b) Landslides triggered by the 22 July 2013 Minxian-Zhangxian, China, Mw 5.9 earthquake: inventory compiling and spatial distribution analysis. J Asian Earth Sci 92:125–142. https://doi.org/10.1016/j.jseaes.2014.06.014

Xu C, Shyu JBH, Xu X (2014c) Landslides triggered by the 12 January 2010 Port-au-Prince, Haiti, Mw = 7.0 earthquake: visual interpretation, inventory compiling, and spatial distribution statistical analysis. Nat Hazards Earth Syst Sci 14(7):1789–1818. https://doi.org/10.5194/nhess-14-1789-2014

Xu C, Xu X, Yao X, Dai F (2014d) Three (nearly) complete inventories of landslides triggered by the May 12, 2008 Wenchuan Mw 7.9 earthquake of China and their spatial distribution statistical analysis. Landslides 11(3):441–461. https://doi.org/10.1007/s10346-013-0404-6

Xu C, Xu X, Shyu JBH (2015a) Database and spatial distribution of landslides triggered by the Lushan, China Mw 6.6 earthquake of 20 April 2013. Geomorphology 248:77–92. https://doi.org/10.1016/j.geomorph.2015.07.002

Xu C, Xu X, Shyu JBH, Gao M, Tan X, Ran Y, Zheng W (2015b) Landslides triggered by the 20 April 2013 Lushan, China, Mw 6.6 earthquake from field investigations and preliminary analyses. Landslides 12(2):365–385. https://doi.org/10.1007/s10346-014-0546-1

Xu C, Xu X, Tian Y, Shen L, Yao Q, Huang X, Ma J, Chen X, Ma S (2016a) Two comparable earthquakes produced greatly different coseismic landslides: the 2015 Gorkha, Nepal and 2008 Wenchuan, China events. J Earth Sci 27(6):1008–1015. https://doi.org/10.1007/s12583-016-0684-6

Xu C, Xu X, Shen L, Yao Q, Tan X, Kang W, Ma S, Wu X, Cai J, Gao M, Li K (2016b) Optimized volume models of earthquake-triggered landslides. Sci Rep 6(1):29797. https://doi.org/10.1038/srep29797

Xu C, Tian Y, Zhou B, Ran H, Lyu G (2017) Landslide damage along Araniko highway and Pasang Lhamu highway and regional assessment of landslide hazard related to the Gorkha, Nepal earthquake of 25 April 2015. Geoenvironmental Disasters 4(1):14. https://doi.org/10.1186/s40677-017-0078-9

C. Xu (✉) · **S. Ma** · **C. Xie**
Key Laboratory of Active Tectonics and Volcano,
Institute of Geology, China Earthquake Administration,
1# Huayanli, Chaoyang District, PO Box 9803, Beijing, 100029, China
Email: xc11111111@126.com; xuchong@ies.ac.cn

Z. Tan
School of Civil Engineering,
Beijing Jiaotong University,
Beijing, 100044, China

S. Toda
International Research Institute of Disaster Science,
Tohoku University,
Aoba, 468-1, Aoba, Sendai, 980-0845, Japan

X. Huang
School of Engineering and Technology,
China University of Geosciences (Beijing),
Beijing, 100083, China